arXiv:physics/0610053v1 [physics.flu-dyn] 9 Oct 2006

Numerical investigations on the finite time singularity in two-dimensional Boussinesq equations

Z. Yin*
National Micrography Laboratory, Institute of Mechanics, Chinese Academy of Sciences, Beijing 100080, P.R.China†

Tao Tang‡
Department of Mathematics, Hong Kong Baptist University, Kowloon Tong, Hong Kong, P.R. China

(Dated: March 31, 2022)

Abstract

To investigate the finite time singularity in three-dimensional (3D) Euler flows, the simplified model of 3D axisymmetric incompressible fluids (i.e., two-dimensional Boussinesq approximation equations) is studied numerically. The system describes a cap-like hot zone of fluid rising from the bottom, while the edges of the cap lag behind, forming eye-like vortices. The hot liquid is driven by the buoyancy and meanwhile attracted by the vortices, which leads to the singularity-forming mechanism in our simulation. In the previous 2D Boussinesq simulations, the symmetricial initial data is used, see, e.g., [20]. However, it is observed that the adoption of symmetry leads to coordinate singularity. Moreover, as demonstrated in this work that the locations of peak values for the vorticity and the temperature gradient becomes far apart as t approaches the predicted blow-up time. This suggests that the symmetry assumption may be unreasonable for searching solution blow-ups. One of the main contributions of this work is to propose an appropriate asymmetric initial condition, which avoids coordinate singularity and also makes the blow-up to occur much earlier than that given by the previously simulations. The shorter simulation time suppresses the development of the round-off error. On the numerical side, the pseudo-spectral method with filtering technique is adopted. The resolutions adopted in this study vary from 1024^2, 2048^2, 4096^2 to 6144^2. With our proposed asymmetric initial condition, it is shown that the 4096^2 and 6144^2 runs yield convergent results when t is fairly close to the predicted blow-up time. Moreover, as expected the locations of peak values for the vorticity and the temperature gradient are very close to each other as t approaches the predicted blow-up time.

*Electronic address: zhaohua.yin@imech.ac.cn

†Part of the work was carried out in Institute of Computational Mathematics, Academy of Mathematics and System Sciences, Chinese Academy of Sciences, Beijing 100080, P.R. China.

‡Electronic address: ttang@math.hkbu.edu.hk

I. INTRODUCTION

The formation of finite time singularities in the three-dimensional (3D) incompressible Euler equations is a controversial subject in fluid mechanics. There are two main reasons for studying the singularity development: firstly, the verification of the finite time singularity may aid to the understanding of the onset of turbulence in slightly viscous flows, and secondly if such singularities do exist then they may provide a means by which energy cascades to and concentrates on small scales.

The equations under consideration are the following:

$$\mathbf{u}_t + \mathbf{u} \cdot \nabla \mathbf{u} + \nabla p = 0, \tag{1}$$

$$\nabla \cdot \mathbf{u} = 0, \tag{2}$$

$$\mathbf{u}(\mathbf{x}, 0) = \mathbf{u}_0, \tag{3}$$

where, $\mathbf{u}$ is the velocity, p is the pressure, $\mathbf{u}_0$ is the given initial velocity which is smooth in the sense that the data reside in some Sobolov space. However, whether the solution $\mathbf{u}$ can remain smooth for all time has yet to be proved.

Since the question of global existence of the 3D incompressible Euler equations has been inaccessible analytically, the question has been investigated numerically in the past two decades. The most commonly used quantity in determining global existence of Eqs. (1)-(3) is the vorticity $\boldsymbol{\omega} = \nabla \times \mathbf{u}$, which has been first developed by Beale, Kato & Majda [1] (also see [2]), and later refined by two other groups [3, 4]. It is shown in [1] that $\mathbf{u}$ will blow up at a finite time T_c if and only if

$$\int_0^t \mid \boldsymbol{\omega}|_{L^\infty} ds \to \infty, \; as \quad t \nearrow T_c \; . \tag{4}$$

This result is especially useful when the question of global existence is numerically investigated, because if we find the maximum norm of the vorticity behaves like $(T_c - t)^{-\alpha}$ with $\alpha > 1$, a finite time singularity has then developed. Based on this theory, three kinds of numerical efforts have been made to search for the singularities in the 3D Euler flows [8, 9, 10, 11, 12, 13, 14, 15, 16, 17, 18]:

1. The original 3D Euler simulation does not adopt symmetric assumption. This scheme requires the largest computer resource.

2. The symmetry introduced by Taylor & Green [5] (see also [6] for some detailed discussion) uses only 1/64 of the total computational time for the non-symmetric case.

3. An even further symmetric technique introduced by Kida [7] requires only 1/192 of the computational time for the non-symmetric case.

In contrast to the 3D research, 2D study is much easier to be performed analytically or numerically. Under the axisymmetric assumption, the 3D Euler equations can be replaced by 2D Boussinesq convection equations. This assumption is an even more aggressive symmetric assumption than the Taylor-Green or Kida flows because it turns this 3D problem into a 2D

one, which can save computer resource significantly. We will give a brief discussion about it in Section II. Similar to the 3D theory, the blowup judgment has been developed for the 2D Boussinesq convection flows [20, 21, 22]. It has been realized that if the maximum absolute values of the vorticity and temperature gradient behave like $(T_c - t)^{-\alpha}$ and $(T_c - t)^{-\beta}$ with $\alpha > 1$ and $\beta > 2$, a finite time singularity will be developed. This simplified 2D model, although lacking of the vortex reconnection as in the 3D simulations [23, 24, 25], can also reveal certain possibility of singularity formation [20, 26, 27, 28, 29, 30, 31, 32].

Among the numerical efforts in addressing the singularity issue, some highest possible resolutions have been attempted in the last two decades. There are mainly two kinds of numerical schemes involved: pseudo-spectral methods and finite differences. For the pseudo-spectral efforts, Kerr used the resolution up to $1024 \times 256 \times 128$ without any symmetric assumption [10], and in a recent work of Hou and Li [19] an extremely fine grid of resolution $1536 \times 1024 \times 3072$ is used. The Taylor-Green or Kida simulations have reached the effective resolution of 1024^3 [12] and 2048^3 [18]. Moreover, the most intensive axisymmetric simulation [20] uses a resolution of 1500^2.

To the best of out knowledge, the most intensive 3D finite difference calculation was performed by Grauer *et al.* [14]. They did not make any symmetric assumption, but used the adaptive mesh refinement (AMR) method to enhance the effective resolution to 2048^3. For the 2D Boussinesq simulation, uniform grids of 512^2 and 1792×1280 were used in [20] and [30], respectively. Pumir & Siggia [28] employed an adaptive 256^2 grid to achieve a resolution of 10^7 in both dimensions. A less aggressive adaptive grid, maybe more accurate due to less frequent re-meshing, uses a 512^2 deformed grid to reach a 4600^2 effective resolution [32].

Besides the numerical efforts mentioned above, the 3D Taylor series analysis, although limited due to the lack of proper parallelized softwares handling high precision calculations, is also used to analyze the 3D Euler singularity problem [33, 34, 35, 36]. Moreover, some analytical studies have been carried out [37, 38, 39, 40, 41, 42, 43, 44, 45, 46], but the original 3D Euler equations have been modified which makes the use of relevant mathematical tools possible, Likewise, some 2D modified Boussinesq equations were also employed in simulations and analysis [47, 48, 49, 50]. Although these models do not have much connection with the original 3D Euler equations, they may provide some hints to the understanding of the singularity issue. One of the latest results was given by Frisch *et al.* [51, 52] who conducted the 2D calculations in the so-called parareal domain by taking the advantages of both spectral and adaptive methods.

One of the main purposes of this work is to investigate how to set up an effective initial condition which can be used in the simulations of the Boussinesq equations. The reason that we emphasize the importance of proper initial conditions is that a poorly chosen initial condition may not lead to blowup or may lead to blowup at a numerically unacceptable large time.

Section II contains a brief discussion on our numerical method. We adopted the so-called phase-shifted technique to do the de-aliasing [53, 54]. It is clear that to a reliable and efficient numerical is very important in simulating possible singular behaviors. Section III gives a quite complete discussion of three initial conditions, including subtle but significant

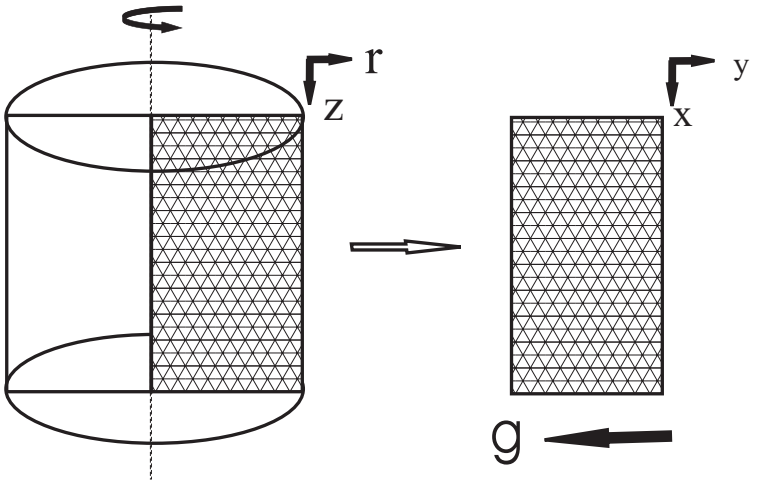


FIG. 1: The analogy between the (r, z) plane in 3D axisymmetric flows with swirl and the (x, y) plane of 2D Boussinesq convection flows. We keep $\mathbf{u} \equiv 0$ near $y = 0$ and $y = 2\pi$ throughout our 2D Boussinesq doubly-periodic calculation to avoid the coordinate singularity in the corresponding 3D axisymmetric flows (see Fig. 3(a)). The solid black arrow at the bottom indicates the direction of the gravity, opposite to the direction of buoyancy.

differences from earlier work. In section V, we use the parallel strategy combined with the traditional parallel FFT and task distribution schemes [55, 56] to solve the 2D Boussinesq equations with resolutions up to 6144^2. The corresponding effective resolution in the 3D Euler formulation is $\pi \times 6144^3 \simeq 9000^3$, which is much finer than any previous efforts. Singularity development will be demonstrated by considering several physical quantities including the peak vorticity and temperature gradient.

II. THE NUMERICAL SCHEME

The connection between the 3D axisymmetric Euler flow with swirl and the 2D Boussinesq convection has been established in [2]. For completeness, we will review the connection briefly.

The basic vorticity equations for the axisymmetric swirling flow in the (r, θ, z) cylindrical coordinates are of the form

$$\frac{\tilde{D}}{Dt}(rv^\theta) = 0, \tag{5}$$

$$\frac{\tilde{D}}{Dt}(\frac{\omega^\theta}{r}) = -\frac{1}{r^4}[(rv^\theta)^2]_z, \tag{6}$$

where

$$\frac{\tilde{D}}{Dt} = \frac{\partial}{\partial t} + v^r\frac{\partial}{\partial r} + v^z\frac{\partial}{\partial z}, \tag{7}$$

$$\omega^\theta = \frac{\partial v^r}{\partial z} - \frac{\partial v^z}{\partial r}. \tag{8}$$

It should be realized that the (z, r) plane is essentially two dimensional flows with (x, y) coordinate system (Fig. 1). By introducing a streamfunction ψ, the 2D inviscid Boussinesq equations have the following form:

$$\theta_t + \mathbf{u} \cdot \nabla\theta = 0, \tag{9}$$

$$\omega_t + \mathbf{u} \cdot \nabla\omega = -\theta_x, \tag{10}$$

$$\Delta\psi = -\omega, \tag{11}$$

where the gravitational constant is normalized to $\mathbf{g} = (0, -1)$, θ the temperature, $\mathbf{u}$ = (u,v) the velocity, $\boldsymbol{\omega} = (0, 0, \omega) = \nabla \times \mathbf{u}$ vorticity, and ψ the stream function. It should be pointed out in the remaining of the work θ is different with that indicated in (5)-(6); it denotes the temperature. Comparing with the pure 2D Euler equations with the streamfunction-vorticity ω-ψ formulation, there is an extra temperature equation, i.e. Eq. (9), and an extra term θ_x associated with the Buoyancy in Eq. (10). Actually, if ω^θ in Eqs. (5-8) is replaced by ω, and $(rv^\theta)^2$ by ρ, a link can be established if we evaluate all external variable coefficients in Eq. (5-8) at $r = 1$. It should be noticed that this link leads to some coordinate singularities under the cylindrical coordinates. Consequently, it is essential to keep the corresponding 2D Boussinesq solutions away from the horizontal boundaries (here, in this paper, $y = 0$ and $y = 2\pi$; see Figs. 1 and Fig. 3(a)).

The method used in our numerical simulation is pseudo-spectral approximations with some proper de-aliasing technique. We also adopt the filtering technique [59] (a careful discussion on filter in turbulence simulations can be found in [60]) to modify the Fourier coefficients such that the stability of the numerical scheme is enhanced. The machine accuracy of our computer with double precision is $\epsilon = 10^{-16} \approx e^{-37}$, and the modifying factor in the filter is $\varphi(k) = e^{-37(2k/N)^{16}}$ for $k < N/2$, where N is the Fourier modes in each direction.

We now briefly discuss the effects of different numerical schemes for the current research. As to be shown later, the main concern is whether or not a δ or δ-like function can be well resolved by using a discrete scheme. It is well known that the spectral coefficients of the δ function is constant for different modes:

$$\delta(x, y) \simeq C \sum_{n=-\frac{N}{2}}^{\frac{N}{2}} \sum_{m=-\frac{N}{2}}^{\frac{N}{2}} e^{-i(nx+my)}, \tag{12}$$

where C is a constant and will be set to 1 in the following. If the resolution $N^2 \to \infty$, we will get the exact Fourier representation. Of course, it is impossible to do this by any computer, and what we can do is to use some finest possible grid (the largest N^2 appearing in the literature is limited to 8192^2 so far [57]). The de-aliasing technique is to remove the aliasing error by setting some of the Fourier coefficients to zero. The filter we adopted is to make some of the Fourier coefficients smaller. So actually, the computer-represented value of the δ function is determined by the resolution N^2, the filter and the de-aliasing.

The de-aliasing scheme to be used is the so-called phase-shift scheme [54], which retains about 7/9 of the total modes. The filter narrows the gap of the peak values of de-aliasing pseudo-spectral schemes and pure spectral schemes. In Table I, the filtering δ function value

TABLE I: Peak values when a $\delta(x, y)$ function is represented by different schemes with the same resolution N^2.

	peak value before filtering	percentage retained by the filter	peak value after filtering
phase-shift	$2\pi N^2/9$	81.3%	$0.568N^2$
No de-aliasing	N^2	59.6%	$0.596N^2$

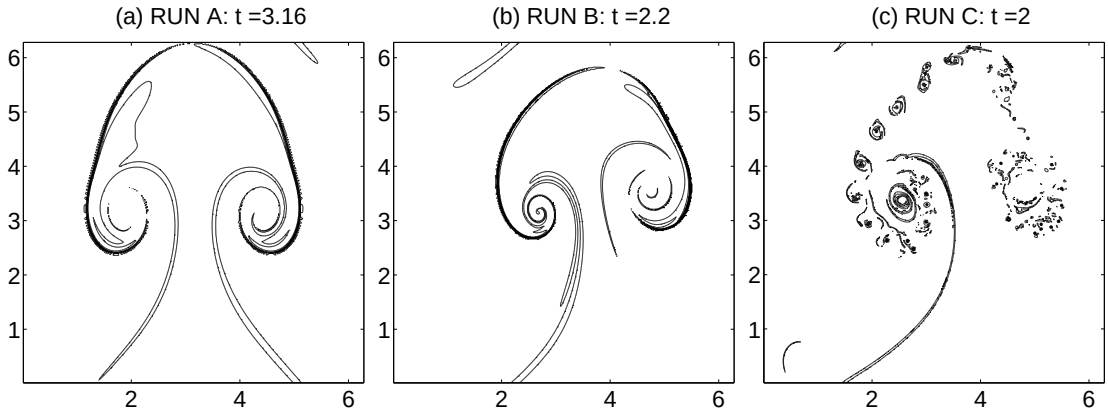


FIG. 2: The vorticity contours of three runs when non-velocity crosses the horizontal boundary. a) and b) are before the blow-up time for RUN A and B, and c) is after the blow-up time of RUN C.

of phase-shift scheme is only 2% lower than the no de-aliasing scheme. In our calculation, we follow the tradition of our pseudo-spectral code (W. H. Matthaeus, private communication) to use the circular truncation in our running [58].

III. INITIAL CONDITIONS

In this paper, three different initial conditions will be considered, which will be named RUN A, RUN B and RUN C, respectively. RUN A adopted the same initial condition as used in Ref [20]:

$$\omega(x, y, 0) = 0, \tag{13}$$

$$\theta(x, y, 0) = 50\theta_1(x, y)\theta_2(x, y)\left[1 - \theta_1(x, y)\right], \tag{14}$$

where if $S(x, y) := \pi^2 - y^2 - (x-\pi)^2$ is positive, $\theta_1 = \exp\left(1 - \pi^2/S(x, y)\right)$, and zero otherwise; if $s(y) := |y - 2\pi| / 1.95\pi$ is less than 1, $\theta_2 = \exp\left(1 - (1 - s(y)^2)^{-1}\right)$, and zero otherwise. By choosing the initial conditions (13)-(14), we can test our discretization schemes by comparing our numerical results with those given in [20].

This governing equations (9)-(11) with the above initial condition have been studied intensively by E & Shu [20] with spectral methods (resolutions: 1500^2) and ENO finite difference methods (resolutions: 512^2). They have predicted that the side part of the rising

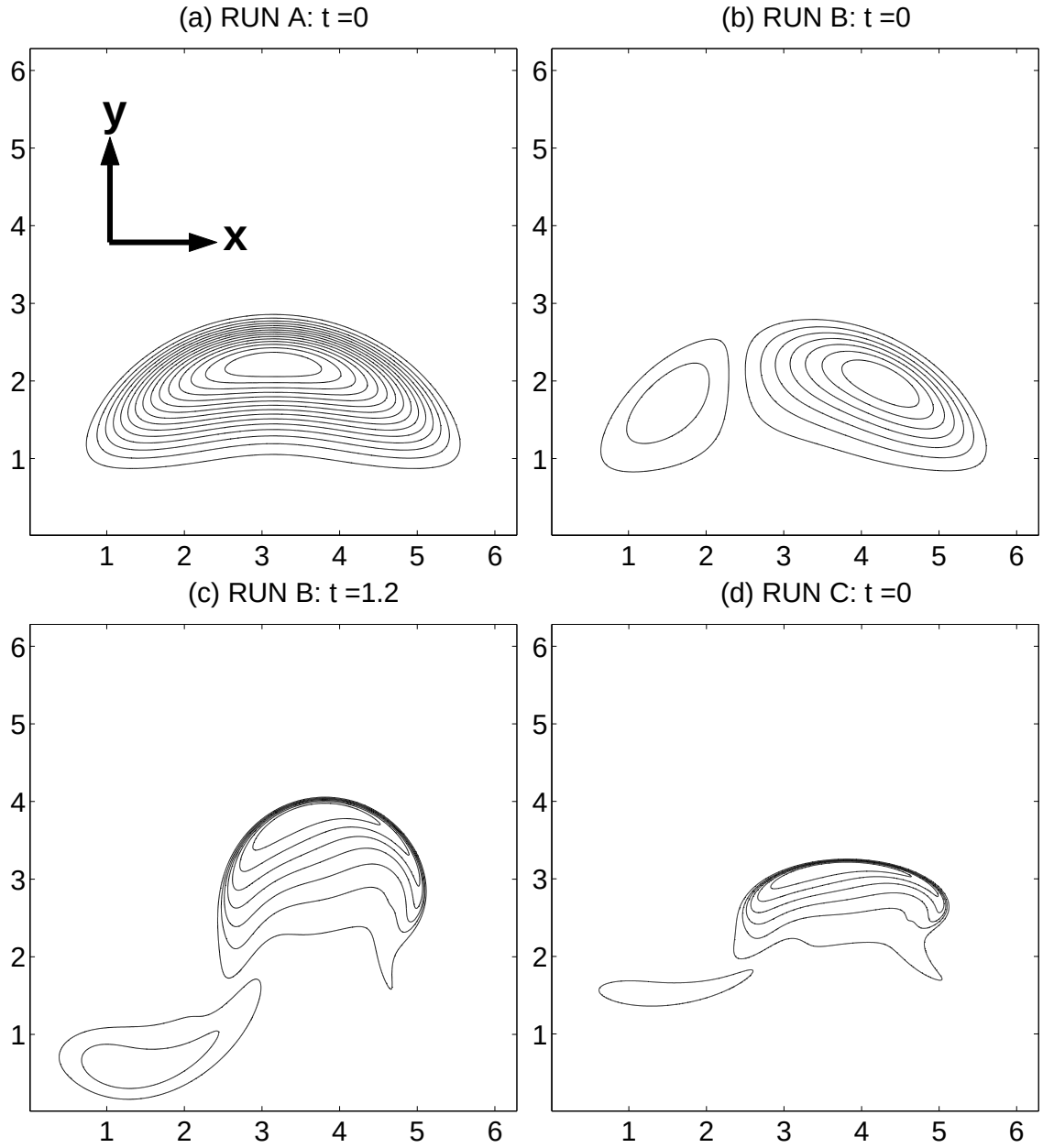


FIG. 3: a), b) and d) are contour plots of temperature for three different initial conditions. d) is obtained after the intermediate results of RUN B (c) are compressed by the factor of 2.

bubble is much more dangerous than the front of the bubble (Fig. 2(a)). However, this initial condition has two shortcomings:

- It introduces another symmetry assumption besides the axisymmetric assumption described in the previous section: the symmetry respect to $x = \pi$ in the (x, y) plane. This will cause a further deviation from the original 3D non-symmetric Euler flows.

- It is demonstrated that the blow-up time of this flow is after $t = 3.16$, at which both $y = 0$ and $y = 2\pi$ are crossed by non-zero velocity, see Fig. 2(a). This is due to the assumption we adopted to simplify the 3D axisymmetric flow to the 2D Boussinesq

flow. In other words, what we are studying here can not be closely related to the 3D Euler flow anymore.

To fix the first difficulty above, we change the initial temperature field in (14) to

$$\theta(x, y, 0) = \frac{50}{\pi}(4x - 3\pi)\theta_1(x, y)\theta_2(x, y)\left[1 - \theta_1(x, y)\right]. \tag{15}$$

The factor $(4x - 3\pi)/\pi$ introduced here is to break the symmetry assumption with respect to $x = \pi$ in the (x, y) plane. However, this simulation (denoted as RUN B) will also cross both $y = 0$ and $y = 2\pi$ (see Fig. 2(b)) before T_c. Therefore, a better initial condition (RUN C) is to compress the intermediate results at $t = 1.2$ obtained in RUN B. More precisely, we let

$$\omega(x, y, 0) = \omega'(x, 2y - 0.4\pi, 1.2), \quad \theta(x, y, 0) = \theta'(x, 2y - 0.4\pi, 1.2), \tag{16}$$

for $(x, y) \in [0, 2\pi] \times [0, \pi]$ (where θ' and ω' are obtained by solving Eqs. (9)-(11), (13) and (15) with a 2048^2 grid), and zero otherwise. The initial condition associated with RUN C is demonstrated in Figs. 3(b, c, d).

There are three main advantages for using the above initial conditions with RUN C:

- There will have no symmetric and boundary crossing problems as observed in RUN A. The flow pattern does not cross the horizontal boundary until $t = 2$ (Fig. 2(c)) while the predicted blow-up time is around $t = 0.91$ (see Section IV B).

- Compared with RUN A, RUN C only needs about 1/4 simulation time to reach the blow-up time T_c, and the advantages of higher resolutions show up at early stages of the simulations. As a result, RUN C can save quite large amount of computational time, which is particularly important in this kind of study.

- Shorter simulation time also suppresses the development of round-off error, which is non-trivial in the current high resolution simulations (see Appendix).

IV. NUMERICAL RESULTS

In this section we will present a detail discussion of the numerical results of RUN A and RUN C. Some features of Run B can be represented by RUN A and C, and will be only briefly discussed. RUN A will serve as a validate run. Moreover, it is used to illustrate some pitfalls we should avoid, such as round-off error, symmetric effect, and coordinate singularity etc. RUN C is the simulation from which we will draw main conclusions.

A. Numerical results for RUN A

For RUN A, three resolutions are used: 1024^2, 2048^2 and 4096^2. The corresponding time steps used are 0.00004, 0.00002 and 0.00001 respectively, given by the CFL condition.

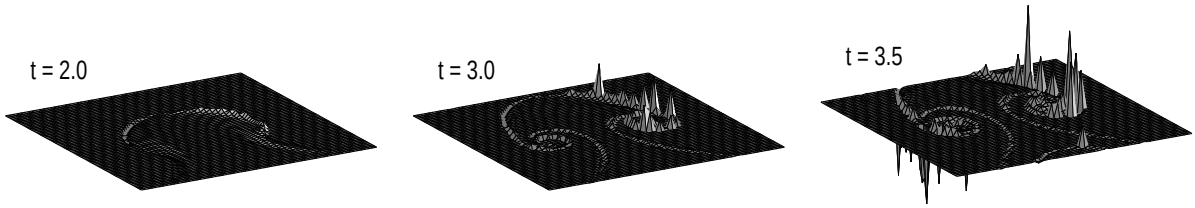


FIG. 4: The 3D perspective plots of vorticity for RUN A with a 4096^2 grid at different times. All 3D effect pictures in this paper (Figs. 4, 5 and 11) are based on smooth flow field.

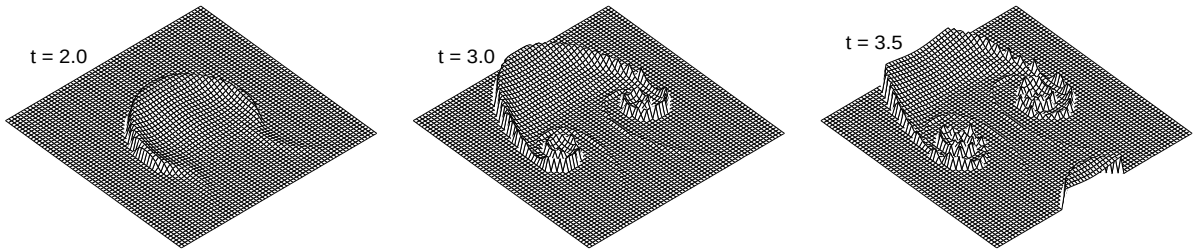


FIG. 5: The 3D perspective plots of temperature for RUN A with a 4096^2 grid.

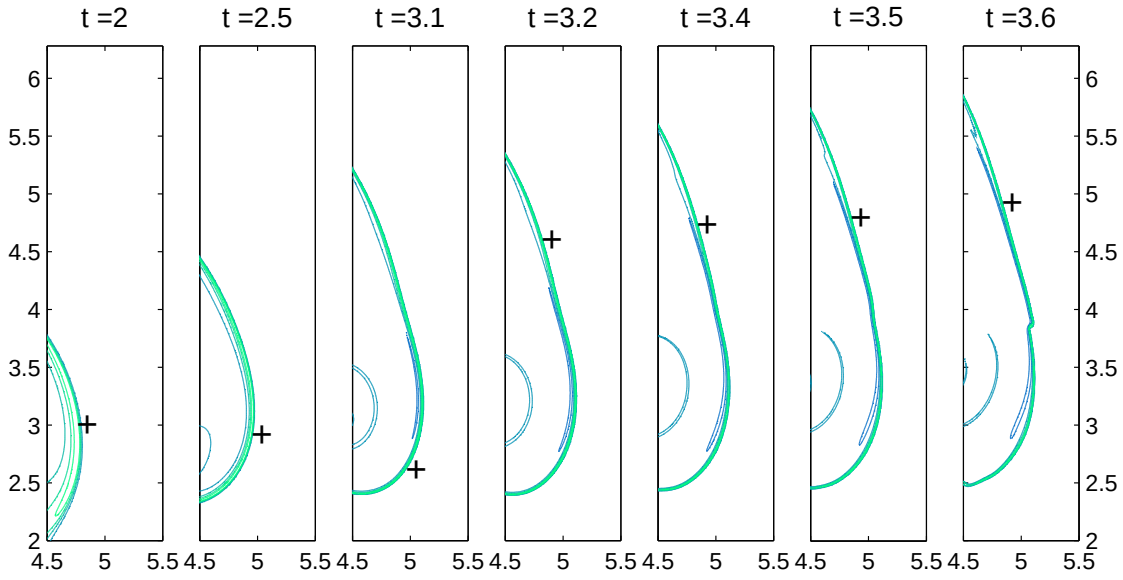


FIG. 6: (Color online). Zoom-in contour plots of vorticity in RUN A at different times with the resolution of 4096^2. Only details near the predicted singularity location ($[4.5, 5.5] \times [2, 2\pi]$) are shown. The plus symbol indicates the location of $|\omega|_{max}$ in the whole $[0, 2\pi] \times [0, 2\pi]$ domain.

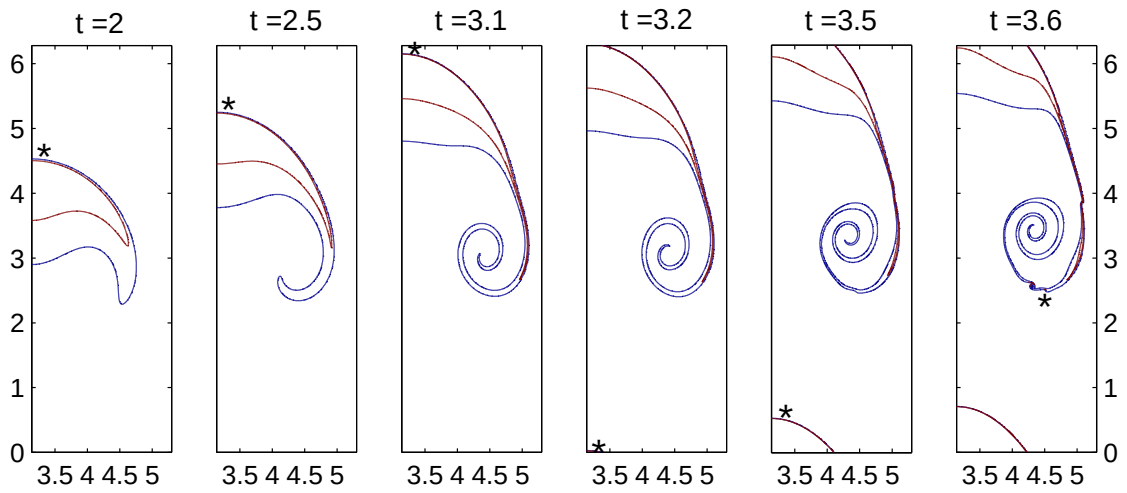


FIG. 7: (Color online). Zoom-in contour plots of temperature in RUN A at different times with the resolution of 4096^2. Only details in $[3.25, 5.3] \times [0, 2\pi]$ are shown. The "$*$" symbol indicates the location of $|\nabla\theta|_{max}$ in the whole $[0, 2\pi] \times [0, 2\pi]$ domain.

At the beginning of the simulations (for all three resolutions), the cap-like initial temperature field (Fig. 3(a)) will rise and develop into a "two-eye" system. Driven by the buoyancy, the vorticity field will also develop from the initially unified zero to a two-eye system, but with one positive and one negative "eyes" this time. Figs. 4 and 5 show the 3D pictures of vorticity and temperature field in the whole domain, and it is clear that the peak values of vorticity are located along the edge of the "eyes."

The system is basically symmetric respect to $x = \pi$ if round-off error does not play a role, so there will have two $|\omega|_{max}$ locations: one positive and one negative. It is worth mentioning that round-off error will spoil this symmetry when very high resolutions are adopted (see the discussion in Appendix). Our highest resolution for RUN A is 4096^2, and the symmetry is well maintained before $t = 3.6$. After $t = 3.6$, the filter spoils the singularity-forming mechanism, and the values of $|\omega|_{max}$ begin to drop when t becomes larger. In the following, we will only use the positive half of the vorticity field (i.e. $x \in [\pi, 2\pi]$) for the divergence analysis.

The "+" symbol in Figs. 6 indicates the locations of $|\omega|_{max}$ at different times. The "+" is around $y = 3$ in the beginning, and suddenly jumps to $y \approx 4.5$ after $t = 3.1$. The flow field has no significant change around $t = 3.1$, and the front of the bubble rises continuously as what happens before that time.

The "*" symbol in Figs. 7 indicates the locations of $|\nabla\theta|_{max}$ at different times. It should be noticed that the tail left behind the rising front is forming an "eye" after $t = 2.5$, and there is a smooth filament connecting the "eye" and the head of the bubble.

The "$*$" symbol jumps to the edges of the forming "eye" around $t \approx 3.6$, roughly at the same time when the original smooth filament breaks up into many even smaller "eyes" (see Figs. 16). This is because our simulation begins to become under-resolved. The filter begins to dramatically reduce the peak values of those δ-like functions. The "*" symbols can not

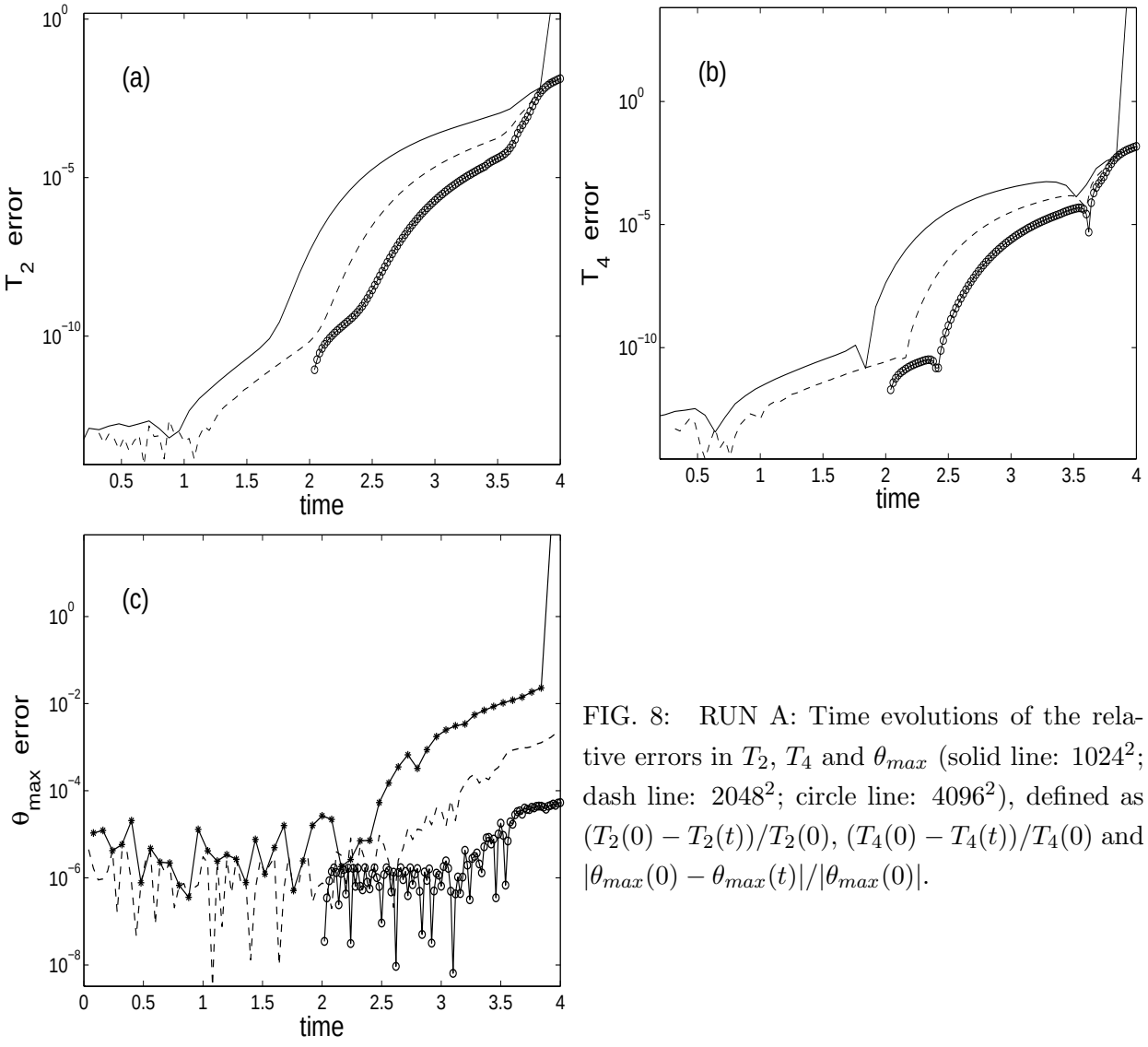


FIG. 8: RUN A: Time evolutions of the relative errors in T_2, T_4 and θ_{max} (solid line: 1024^2; dash line: 2048^2; circle line: 4096^2), defined as $(T_2(0) - T_2(t))/T_2(0)$, $(T_4(0) - T_4(t))/T_4(0)$ and $|\theta_{max}(0) - \theta_{max}(t)|/|\theta_{max}(0)|$.

represent the exact maximum locations of the 2D Boussinesq solution anymore. The edge of temperature contour is very smooth before the collapsing time, and the front part of the rising bubble and the two eyes left behind (Figs. 5) stretch the filament connecting them.

Questions arise as to how effectively the large local quantity (in our case, the vorticity and temperature gradients) can be resolved and how much the results vary with resolution. It is evident that for the extreme hypothetical case, when one of the local quantities is a delta function, it can only be resolved with infinite resolution. To resolve an ideal shock wave (with zero thickness), for example, in the absence of any smoothing, needs infinite number of grid points. In the following, we will check several other aspects on the effectiveness of the numerical simulations, mainly by finding some quantity properties useful in demonstrating the effect of the mesh refinement, or identifying the trend when high resolutions are adopted.

First, we check the following three values which are time independent due to the divergence-free constraint, the doubly-periodic condition and the inviscid transport equation (Eq. (9)):

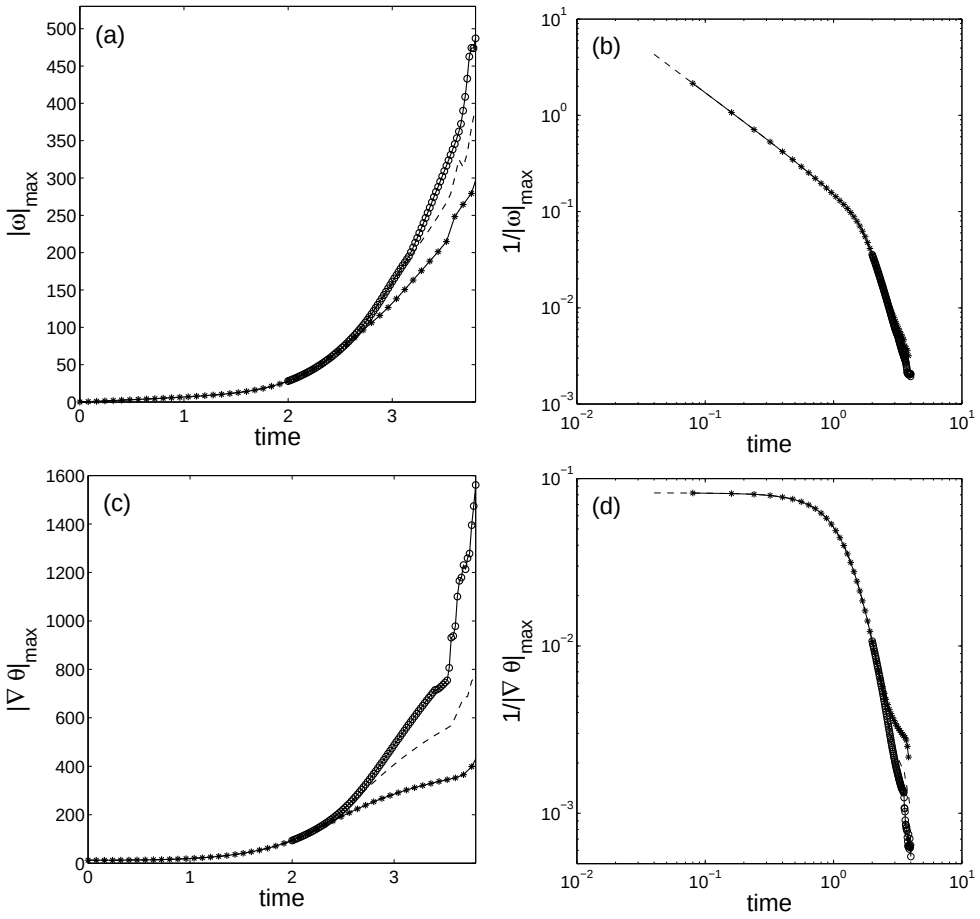


FIG. 9: RUN A: Time evolution of $|\omega|_{max}$ and $|\nabla\theta|_{max}$ (solid line: 1024^2; dash line: 2048^2; circle line: 4096^2).

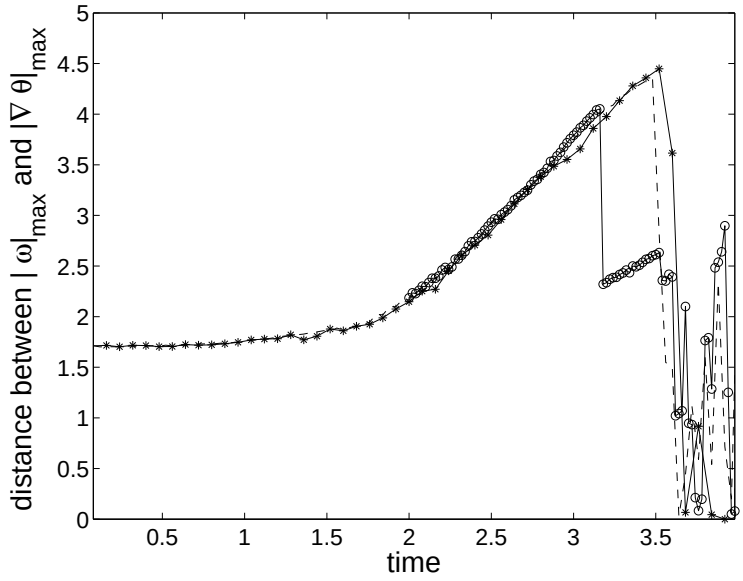


FIG. 10: RUN A: The distance between the locations of $|\omega|_{max}$ and $|\nabla\theta|_{max}$ at different times for three kinds of resolutions (solid line: 1024^2; dash line: 2048^2; circle line: 4096^2).

- $T_2(t) = \int_0^{2\pi} \int_0^{2\pi} \theta^2(x, y, t) dx dy$,
- $T_4(t) = \int_0^{2\pi} \int_0^{2\pi} \theta^4(x, y, t) dx dy$, and
- $\theta_{max}(t)$

Fig. 8 shows that the global average quantities are well conserved within 1% error for 4096^2 and 2048^2 resolutions throughout the entire simulation period $t \in [0, 4]$. To save the computation time, our 4096^2 run starts from $t = 2.0$ using the intermediate result of 2048^2, so for 4096^2 run, those errors are defined as $(T_2(2.0) - T_2(t))/T_2(2.0)$, $(T_4(2.0) - T_4(t))/T_4(2.0)$ and $|\theta_{max}(2.0) - \theta_{max}(t)|/|\theta_{max}(2.0)|$.

The 1024^2 run has a very poor performance after $t = 3.8$ because none of these relative errors are below 10%. The performance of 2048^2 run is almost as good as on 4096^2 grid by considering T_2 and T_4, with under 1% relative errors. However, the relative errors on θ_{max} of 4096^2 are always below 10^{-4}, which are only about 2% of the errors in 2048^2 simulation after $t = 3.5$ (Figs. 8(c)). These errors give some indicators on how far the numerical solution is away from the real one.

Figs. 8(a) and (b) show that T_2 and T_4 errors of 4096^2 run are always lower than those given by the 1024^2 and 2048^2 simulations. However, due to the round-off error in our calculations (see Appendix), this is not the case for θ_{max} error (Figs. 8(c)), because the errors associated with the 4096^2 resolution seems to be at the same level of those with the 2048^2 resolution from $t = 2.0$ to $t = 2.6$. When t is close to the blow-up time, the 4096^2 run conserves the value of θ_{max} much better than other runs. In fact, when $t \to T_c$, the truncation error will overwhelm the influence of machine precision, and higher resolutions have more advantages than lower ones. For future simulations, however, we may have to take some measures to control the round-off error when refined grids are used, say, the quadruple precision (the machine accuracy $\epsilon = 10^{-32}$) may be used to replace the present double-precision ($\epsilon = 10^{-16}$). On the other hand, the present results of 2048^2 and 4096^2 simulations seem to be accurate enough to draw some conclusions in the blow-up analysis.

Figs. 9(a) and (c) show the time evolutions for $|\omega|_{max}$ and $|\nabla\theta|_{max}$ with different resolutions. We re-plot these maximum value evolutions in Figs. 9(b) and (d) with logarithmic scales. It seems that the growth of $|\omega|_{max}$ and $|\nabla\theta|_{max}$ in the 4096^2 run terminates in a finite time with $|\omega|_{max} \sim (T_c - t)^{-1.23}$ and crudely $|\nabla\theta|_{max} \sim (T_c - t)^{-2.48}$. The corresponding predicted blow-up time is $T_c = 3.72$. Even for 2048^2 run, there is an obvious trend towards the singularity.

However, there are still two facts that cause suspects of this conclusion:

- The simulation never reaches the blow up time T_c;
- Even for the 4096^2 run, we can not say that we have resolved the problem confidently because the time-evolution curves for $|\omega|_{max}$ and $|\nabla\theta|_{max}$ show quite large differences between high and low resolutions at late stages of the simulations.

The first point is unavoidable due to the discrete nature of the numerical simulations. The second point may be improved by employing higher resolution, or, at least we can extend

the overlapping region to a time closer to T_c. For example, the $|\omega|_{max}(t)$ lines of 1024^2 and 2048^2 runs diverge around $t = 2.7$, but the 2048^2 and 4096^2 curves diverge around $t = 3.2$. However, the effort in this direction may be useless because, as explained in the following paragraph, we can not get a clearer physical picture of the singularity forming mechanism even we use higher resolution.

Physically speaking, if a singularity is about to form at $t = T_c$ on the point (x_c, y_c), the locations of $|\omega|_{max}$ and $|\nabla\theta|_{max}$ should approach (x_c, y_c) when $t \to T_c$. This means the distance between the locations of these two peak values should become smaller and smaller as $t \to T_c$. Although it is impossible for any numerical solver to reach T_c, we can use this property to check whether a numerical simulation reflects the physical mechanism properly. Fig. 10 shows that the locations of $|\omega|_{max}$ and $|\nabla\theta|_{max}$ in RUN A initially stay far away from each other (about 1.7 length unit in the $[0, 2\pi] \times [0, 2\pi]$ domain) and they do not get closer when the "singular" time is approaching [67]. The distance are noticeably increased after $t \approx 1.7$ for all three resolutions. When $t \in [3.2, 3.5]$, it is even wider (see also the specific locations of those maximum values in Figs. 6 and 7). The physical mechanism behind it is very unclear, maybe because the numerical code is trying to preserve the symmetry from the very beginning of flow pattern (Chapter 2 of [66]), accompanied by the singularity forming mechanism. It seems that there are at least two locations at which the singularity is formed simultaneously at $x \in [\pi, 2\pi]$, fighting for the locations of global maximum values. Because the divergent conclusion drawn from Figs. 9(b) and (d) means nothing unless higher resolutions are adopted, we should consider some other initial condition which may reveal more physical phenomena more effectively. The results of RUN A seem too complicated to be analyzed.

To sum up for this subsection, we basically end up with similar conclusion as in [20] in the sense that the edge of the "cap" is more dangerous than the front. Although our code can resolve the 2D Boussinesq equations accurately until about $t \approx 3.5$ on the 4096^2 grid, we can not obtain a clear physical picture relevant to the singularity issue for the 3D Euler equations. RUN A can only be used to reveal some singular phenomena in the 2D Boussinesq equations.

B. Numerical results for RUN C

In RUN C, we use four sets of grids, namely 1024^2, 2048^2, 4096^2 and 6144^2. The corresponding time steps are 0.00004, 0.00002, 0.00001 and 0.000008 respectively (for 4096^2 run, we use $\Delta t = 0.00002$ for $t < 0.22$, and 0.00001 for $t \geq 0.22$ to save the computation time).

Fig. 11 shows the 3D pictures of vorticity in the whole domain of RUN C. The rising bubble also develops into two "eyes" like that in RUN A. In RUN C, as a whole, the positive "eye" has much larger absolute values for $|\omega|$ and $|\nabla\theta|$ than those of the negative "eye." There is no symmetry with respect to $x = \pi$ anymore. In the following, we will only exam the details around the positive "eye" with a particular attention to the locations of the global maximal $|\omega|$ and $|\nabla\theta|$ (see Fig. 12).

A noticeable difference between Fig. 12 and Fig. 6 is about the location for $|\omega|_{max}$. For

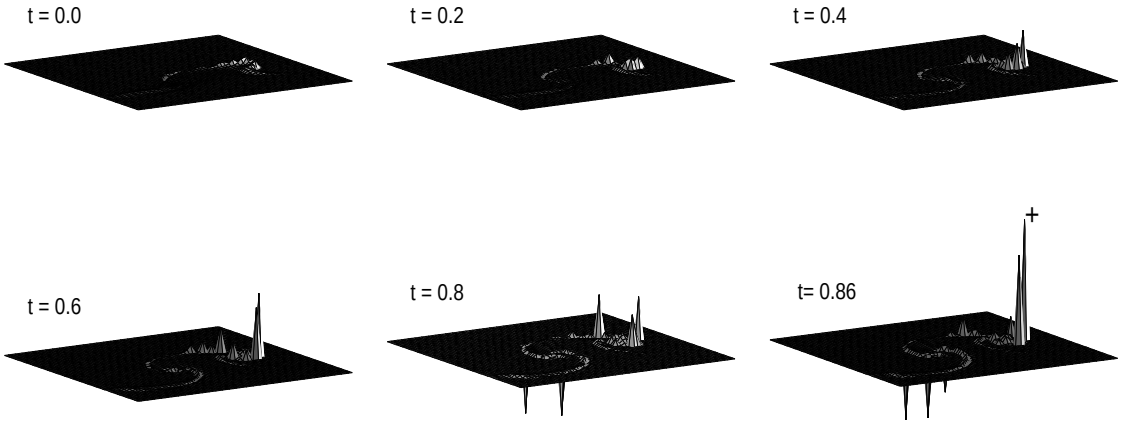


FIG. 11: The 3D perspective plots of vorticity for RUN C with the 6144^2 grid.

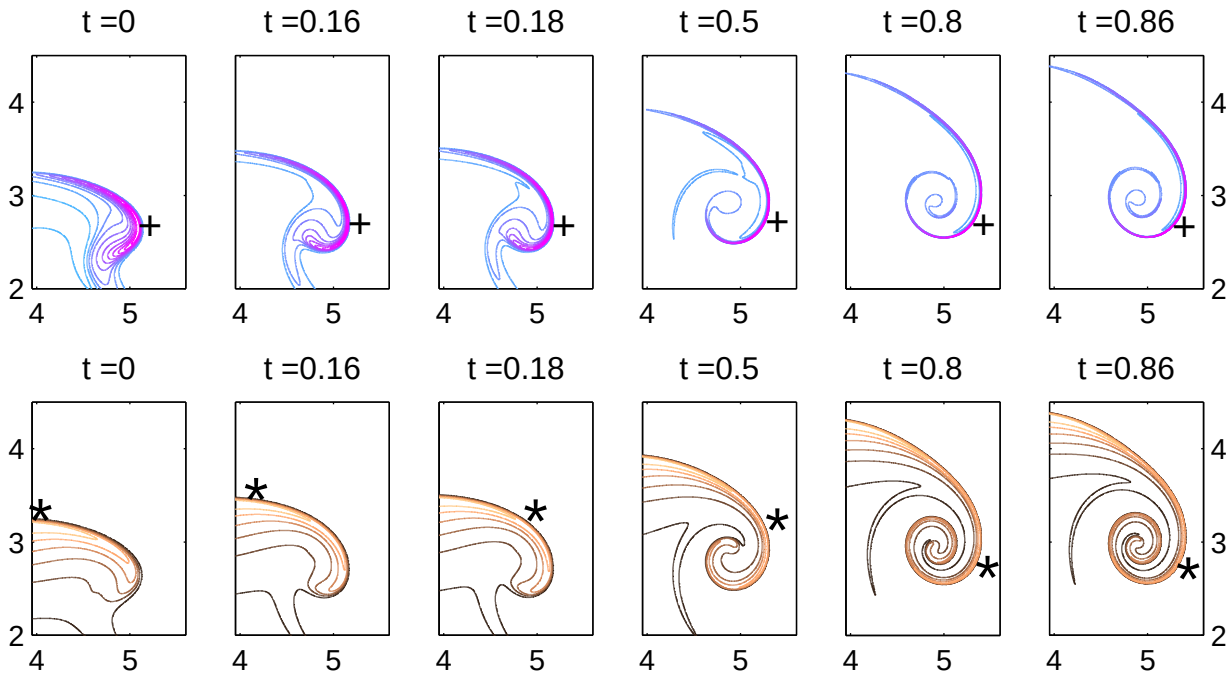


FIG. 12: (Color online). Zoom-in contour plots of vorticity (the first row) and temperature (the second row) in RUN C at different times with the resolution of 4096^2. The "+" and "*" indicate the location of $|\omega|_{max}$ and $|\nabla\theta|_{max}|$ in the whole $[0, 2\pi] \times [0, 2\pi]$ domain, respectively.

RUN C, from the very beginning until the collapsing time ($t \approx 0.88$), the location of $|\omega|_{max}$ is changing continuously and smoothly without any noticeable jumping. This is quite different to the sudden jumping of "+" symbol in RUN A at $t \approx 3.2$. The $|\nabla\theta|_{max}$ is located around $x \approx 4$ in the beginning (until $t \approx 0.16$, see "$*$" in Fig. 12), right on the head of the rising

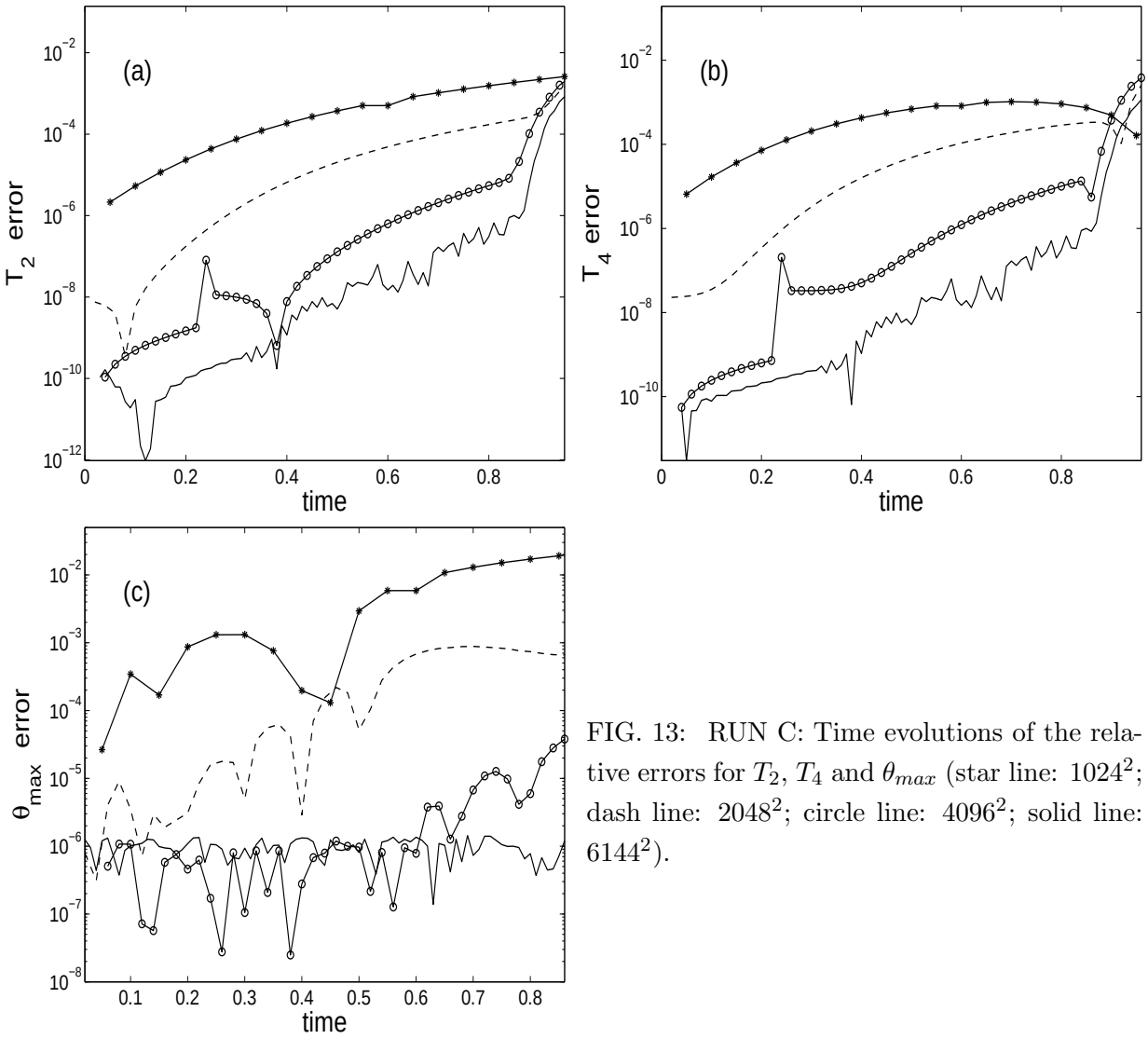


FIG. 13: RUN C: Time evolutions of the relative errors for T_2, T_4 and θ_{max} (star line: 1024^2; dash line: 2048^2; circle line: 4096^2; solid line: 6144^2).

bubble (in this sense, it behaves like RUN A).

The "*" jumps to $x \approx 5$ at $t \approx 0.18$, roughly at the same time when the "eye-like" vortex begins to form. Afterwards, the "*" symbol moves quite continuously towards the location of $|\omega|_{max}$. After $t = 0.7$, the locations of $|\omega|_{max}$ and $|\nabla\theta|_{max}$ are very close to each other. In the meanwhile, the filament connecting the cap front and the "eye" in the temperature field becomes thinner and thinner, which breaks down after $t = 0.87$ due to insufficient resolutions.

For the three low resolutions (1024^2, 2048^2 and 4096^2), the time evolutions of the three time independent values $T_2(t)$, $T_4(t)$ and $\theta_{max}(t)$ in RUN C (Fig. 13) are quite similar to the results in RUN A (Figs. 8). Because shorter simulation time is needed, the 4096^2 result of RUN C is less affected by the round-off error. As a result, the 4096^2 curve is always below those of two lower resolutions, see Fig. 13(c). The truncation error is the main source of the error for these three low resolutions.

Furthermore, if we we only look at errors of T_2 and T_4, the 6144^2 results show much

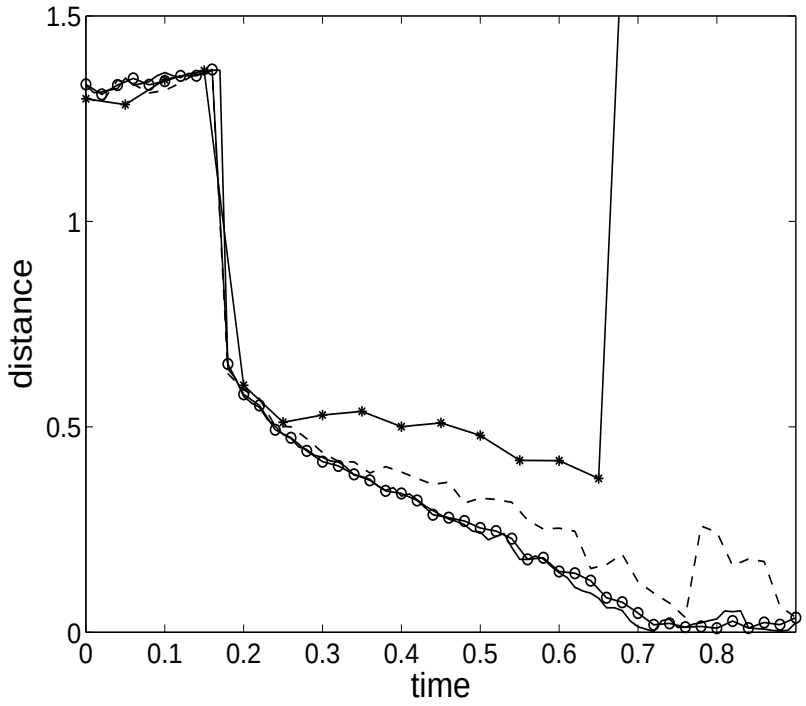


FIG. 14: RUN C: The distance between the locations of $|\omega|_{max}$ and $|\nabla\theta|_{max}$ at different times with four resolutions (star line: 1024^2; dash line: 2048^2; circle line: 4096^2; solid line: 6144^2).

better conservation property than that of the three coarser grids (Figs. 13(a) and (b)). The θ_{max} error, which is more easily affected by the round-off error, shows no advantage of finer grids (Figs. 13(c)): for $0 \leq t \leq 0.6$ the error of the 6144^2 resolutions is at the same level as that of the 4096^2 resolution. However, when $t > 0.6$, the advantage of the 6144^2 resolution is observed: the error of θ_{max} remains around 10^{-6} which is one order lower than that of the 4096^2 result. The round-off error of 6144^2 can roughly match the truncation error. This indicates that it seems necessary to employ quadruple precision instead of the double precision if extremely finer resolutions (say 10^5 in each dimension) are used.

Again, we investigate the time evolution of the distance between the locations of $|\omega|_{max}$ and $|\nabla\theta|_{max}$ under the same resolution. Unlike the RUN A case (see Fig. 10), we obtain a very clear physical picture (Fig. 14). Around $t = 0.2$, the distance experiences a sudden drop, and then decays slowly. The 1024^2 curve has an early dramatic increase at $t \approx 0.65$ due to under-resolution. The results of the 4096^2 and 6144^2 resolutions are quite satisfactory since the distance remains small. The finest resolution shows no obvious advantage here. For RUN A, the first-time jump of "+" (Figs. 6) is followed by the increasing distance between the locations of $|\omega|_{max}$ and $|\nabla\theta|_{max}$ (see Fig. 10). For RUN C, however, it seems that the singularity forming mechanism is the main driving source, which leads to the decreasing distance between the locations for $|\omega|_{max}$ and $|\nabla\theta|_{max}$ after the first jump of "+".

Now we can analyze the singularity forming mechanism of RUN C. We focus on the filament connecting the cap front and the right "eye-like" vortex (see, for example, the temperature contour plot at $t = 0.8$ in Figs. 12). The filament corresponds to the hotter

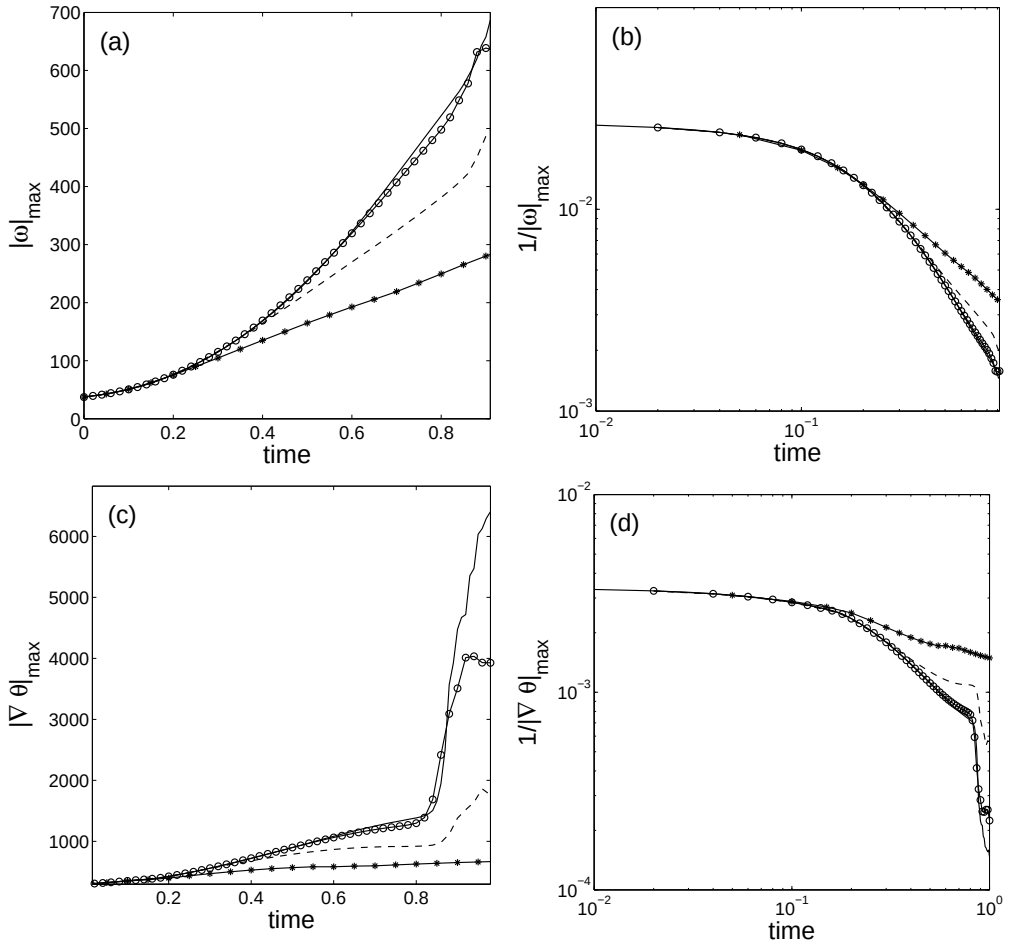


FIG. 15: RUN C: Time evolution of $|\omega|_{max}$ and $|\nabla\theta|_{max}$ (star line: 1024^2; dash line: 2048^2; circle line: 4096^2; solid line: 6144^2).

region of the fluid field, which will rise due to the buoyancy without any other forces. On the other hand, the forming "eye" tries to absorb the fluid around it. These two mechanisms fight with each other, which makes the filament thinner and thinner until singularity appears. For RUN A, besides these two mechanisms, there is a third one joining the competition, namely, the symmetry with respect to $x = \pi$. The third mechanism is not physical, but the numerical scheme tends to preserve it throughout the simulations. With three mechanisms working simultaneously, it is difficult to know when and where the singularity will be formed, although the time evolutions of $|\omega|_{max}$ and $|\nabla\theta|_{max}$ give some hints on solution blow-up. In contrast, the locations of $|\omega|_{max}$ and $|\nabla\theta|_{max}$ in RUN C are getting closer and closer when the solutions become singular.

We now think it is safe to carry out some singularity analysis for RUN C. Figs. 15(a) and (c) show the time evolutions for $|\omega|_{max}$ and $|\nabla\theta|_{max}$ in different resolutions; the inverse of the maximum values are plotted in Figs. 15(b)(dnd). In the following, we will pay our attention to the 4096^2 and 6144^2 curves, because these two lines seem to be overlapping until around $t = 0.88$.

For the 4096^2 run, there are some very small vorticity structures which begin to appear at $t = 0.84$ in the lower part of the smooth outer layer where the maximum $|\omega|$ turns up. For 6144^2 run, this happens at $t \geq 0.87$. After this critical time, the filter we adopted in the

codes removes more and more energy from the system. Consequently, the global average values like T_2 are greatly affected. As a result, our numerical results after $t \geq 0.87$ may not be reliable. Actually, it is observed that the $|\omega|_{max}$ and $|\nabla\theta|_{max}$ experience a drop-down after $t \simeq 0.9$. This indicates that the filter prevents the occurrence of the blowup of the maximum vorticity, which is similar to the viscosity effect in high Reynolds number simulations (e.g. [12]). For the 1024^2 and 2048^2 runs, however, the drop-downs appear later than $t \simeq 0.88$ and the blow-up time T_c is also delayed.

Only the sample maximum values before $t = 0.86$ in 6144^2 run will be used in the singularity analysis because before this critical time convergence between the 4096^2 and 6144^2 results is observed. With a statistical weighted least square fitting for the data after $t = 0.6$, we conclude that the growth of $|\omega|_{max}$ and $|\nabla\theta|_{max}$ for RUN C terminates in a finite time with $|\omega|_{max} \sim (T_c - t)^{-1.12}$, and crudely $|\nabla\theta|_{max} \sim (T_c - t)^{-2.38}$ with $T_c = 0.91$.

There seems to have a trend of singularity also for the 2048^2 run, and the 1024^2 result indicates no blow-up. Moreover, the collapsing times for higher resolutions are earlier than those of lower ones because the filter removes more energy with low resolutions, retarding the singularity forming mechanism.

It should be noticed that the peak vorticity we obtained is the value modified directly by the filter, and the highest peak of the δ-like function (see the peak near "+" in Fig. 11 when $t = 0.86$) is reduced significantly. On the other hand, $|\nabla\theta|_{max}$ is less affected by the filter because it is the temperature field being filtered (not the $\nabla\theta$ field). No place in the temperature field is really close to a δ-function. Hence, the temperature filed is less affected by the filter than the vorticity field. From this point of view, the $|\nabla\theta|_{max}$ curve is more accurate than the $|\omega|_{max}$ one. If there is a blow-up in the simulation, the $|\nabla\theta|_{max}$ curve will show a stronger divergent tendency than the $|\omega|_{max}$ one (Figs. 15).

We have not performed the simulation on grids finer than 6144^2, but we can predict some results from the present computations. It is well known that when a delta function is approximated by a finite number of Fourier modes, each doubling of the resolutions will cause doubling of the maximum value and 2^{n+1} times the maximum values of the n^{th}-order space derivative (see the analysis in Appendix A of [12]). In the final state of our simulation (Fig. 12 (t=0.86)), the cut-line at $y = 2.72$ through the out-layer of the "eye" of the vorticity field looks very similar to a delta function. Therefore, when finer and finer resolutions are used the peak vorticity and temperature gradient are getting larger and larger. From this point of view, further 2D Boussinesq simulations with even higher resolutions will support our singularity prediction although it seems impossible for any code to reach the same T_c if the current filtering relevant scheme is used.

V. DISCUSSIONS AND CONCLUSIONS

There have been extensive discussions on the 3D Euler singularity with viscous simulations by using the Taylor-Green vortex and high symmetry flows (the most intensive one, in our opinion is [12]). As the Reynolds number is increased, the amplitudes of the maximum vorticity, skewness, and flatness increase, and the peaks are attained at earlier times. This is

quite similar to what happens to our simulation with the filter. Our simulation also reaches an earlier "blow-up" when higher resolutions are adopted. These tendencies give hints that for the pure inviscid case (no viscosity or filter), all these quantities may blow up.

A natural question is to discuss what is the influence with symmetry assumptions. We tend to believe that for the Taylor-Green, high-symmetry Kida and axisymmetric flow, all the symmetry constraints are unstable, and in the absence of symmetries, the flow will escape from the singularity formation direction. Moreover, singularity formations depend strongly on how the initial conditions are set up. The numerical method chosen has also a strong impact on the results. For example, finite difference simulations that do not make use of any symmetry produce no singularity indication [27] , whereas Fourier-Chebyshev [10] simulations with symmetry constraints suggest singular trends.

To sum up, we follow the track of [20], and end up with a more developed result. The disagreement between the locations of $|\omega|_{max}$ and $|\nabla\theta|_{max}$ suggests that the symmetric initial data proposed in [20] may not be appropriate (see Fig. 10). To fix this problem, a new initial condition is proposed in this work, which enables us to make some fine grid simulations.

There are several points that make us believe that there is a singularity in RUN C:

- Our simulations show that the time evolution curves of $|\omega|_{max}$ and $|\nabla\theta|_{max}$ become steeper when the grids are refined.
- The distance between $|\omega|_{max}$ and $|\nabla\theta|_{max}$ on the 6144^2 and 4096^2 grid shows a convergent behavior near T_c.
- The distance between the locations of $|\omega|_{max}$ and $|\nabla\theta|_{max}$ is small even up to the predicated blow-up time.

Acknowledgments

We would like to thank Prof. Linbo Zhang for the support of using the *Lenovo* Deepcom 1800 parallel computer in the Institute of Computational Mathematics of the Chinese Academy of Sciences. This work was supported by National NSF of China (G10502054 and G10476032). ZY thanks Professors Ruo Li, Zhenhuan Teng, Jie Shen, Wenrui Hu and Qi Kang for useful discussions. TT thanks the support from the International Research Team on Complex System of the Chinese Academy of Sciences and from the Hong Kong Research Grant Council.

APPENDIX: THE EFFECT OF FILTER ON ROUND-OFF ERROR

The influence of round-off errors on computation has been observed and noticed for a long time, probably starting from the appearance of the digital computer. The round-off error starts to occur at the very beginning of all numerical simulations, and can be amplified by the time integration procedure. A comprehensive study on how machine precision can affect the dynamic simulation is carried out in [61]. Later, in vortex sheet roll-up simulations, a

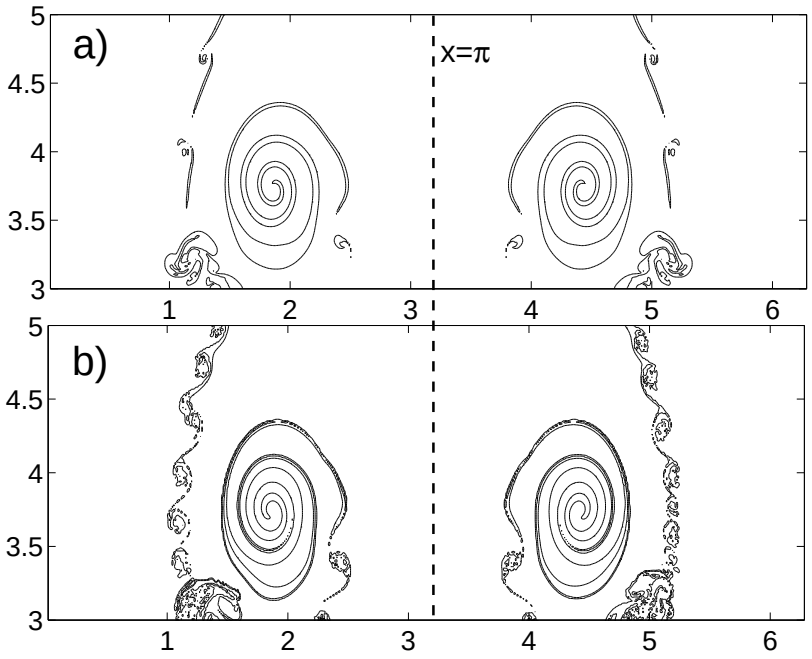


FIG. 16: RUN A: Contour plots of temperature and vorticity at different times with the resolution of 4096^2.

practical result about these effects with two kinds of precisions (7 and 14-digit arithmetic) is presented [62]. In the following, we will try to give a brief analysis about the round-off error in our simulations.

There are three ways to accumulate round-off errors in our simulations:

1. Fast Fourier Transform (FFT) can control the initial round off error very well. Through the result in [63, 64], we can roughly guess that the error is amplified about 100 times for current resolutions ($1024^2 - 4096^2$), that is, the error will be in order of 10^{-13} if the double precision ($\varepsilon = 10^{-15}$) is adopted. The 4096^2 grid will have only slightly larger round-off error than that of 1024^2 grid (only a factor of $log4096/log1024 \approx 1.2$, based on the worst possibility given in [63]).

2. The filtering technique we adopted can significantly amplify the round-off error. According to [65], the filter will amplify the round-off error by a factor of $(\sum c_k^2)^{\frac{1}{2}}$. Here, c_k is the factor added onto the Fourier coefficients by the filter. Actually, most of c_k are 1, so roughly speaking, the round-off error will be enlarged by N times for a N^2 simulation. This means our 1024^2 run will have a 10^{-10} error for each time step, and the error in 4096^2 runs is four times larger.

3. Remember that the analysis above only happens within each time step, and the real round-off error can be even larger in a dynamic run. The time step of 4096^2 run is 1/4 of the 1024^2 run according to the CFL condition, which means 4096^2 needs four times as many time steps as 1024^2.

As a whole, for the same simulation, the round-off error in 4096^2 run will be $1.2 \times 4 \times 4 = 19.2$ times larger than that in 1024^2 run. This difference is already big enough to break the initial symmetry maintained by the numerical solver. Fig. 16(a) is the contour plot of RUN

A at $t = 4.0$ with the 1024^2 grid, which has less details and level than the 4096^2 grid (Fig. 16(b)). However, Fig. 16(a) preserves the symmetry respect to $x = \pi$ very well, while Fig. 16(b) has a different number of vortices on the left and right sides of the picture. In the main text, a discussion of the round-off error is also carried out together with Figs. 8 and 13, focusing on the round-off error amplified by the time evolution.

Figs. 16 are results after the simulation becomes under resolved. Our 4096^2 simulation of RUN A is very symmetric respect to $x = \pi$ before $t = 3.5$. The round-off error in 6144^2 will be about 30 times larger than that of the 1024^2 run. The round-off error is not negligible comparing with truncation error for 6144^2 run (Fig. 13(c)), it seems a must to adopt quadruple precision on a finer grid.

---

[1] J.T. Beale, T. Kato & A. Majda, Remarks on the breakdown of smooth solutions for the 3-D Euler equations, *Commun. Math. Phys.* **94**, 61 (1984).

[2] A.J. Majda & A.L. Bertozzi, *Vorticity and incompressible flow* (Cambridge, 2002).

[3] G. Ponce, Remarks on a paper by J.T. Beal, T. Kato, and A, Majda, *Commun. Math. Phys.* **98**, 349 (1985).

[4] H. Kozono & Y. Taniuchi, Limiting case of the Sobolev inequality in BMO with application to the Euler euuations, *Commun. Math. Phys.* **214**, 191 (2000).

[5] G.I. Taylor & A.E. Green, Mechanism of the production of small eddies from large ones, *Proc. Roy. Soc. A* **151**, 421 (1935).

[6] M.Brachet, D.I. Meiron, S.A. Orszag, B.G. Nickel, R.H. Moft & U. Frisch, Small-scale structure of the Taylor-Green vortex, *J. Fluid Mech.* **130**, 411 (1983).

[7] S. Kida, Three-dimensional periodic flows with high-symmetry, *J. Phys. Soc. Japan* **54**, 2132 (1985).

[8] C. Sulem, P.L. Sulem & H. Frish, Tracing complex singularity with spectral methods, *J. Comput. Phys.* **50**, 138 (1983).

[9] M.E. Brachet, M. Meneguzzi, A. Vincent, H. Politano & P.L. Sulem, Numerical evidence of smooth self-similar dynamics and possibility of subsequent collapse for three-dimensional ideal flows, *Phys. Fluids A* **4**, 2845 (1992).

[10] R.M. Kerr, Evidence for a singularity of the three-dimensional, incompressible Euler equations, *Phys. Fluids A* **5**, 1725 (1993).

[11] S. Tanveer & C.G. Speziale, Singularities of the Euler equation and hydrodynamic stability, *Phys. Fluids A* **5**, 1456 (1993).

[12] O.N. Boratav & R.B. Pelz, Direct numerical simulation of transition to turbulence from a high-symmetry initial condition, *Phys. Fluids* **6**, 2757 (1994).

[13] R.B. Pelz, Locally self-similar, finite-time collaps in a high-symmetry vortex filament model, *Phys. Rev. E* **55**, 1617 (1997).

[14] R. Grauer, C. Marliani & K. Germaschewski, Adaptive mesh refinement for singular solutions of the incompressible Euler equations, *Phys. Rev. Lett.* **80**, 4177 (1998).

[15] R.B. Pelz, symmetry and the hydrodynamic blow-up problem, *J. Fluid Mech.* **444**, 299 (2001).
[16] R.M. Kerr, Vortex collapse and turbulence, *Fluid Dyn. Res.* **36**, 249 (2005).
[17] R.M. Kerr, velocity and scaling of collapsing Euler vortices, *Phys. Fluids* **17**, 075103 (2005).
[18] C. Cichowlas & M. Brachet, Evolution of complex singularities in Kida-Pelz and Taylor-Green inviscid flows, *Fluid Dyn. Res.* **36**, 239 (2005).
[19] T. Y. Hou & R. Li, Dynamic depletion of vortex stretching and non-blowup of the 3-D incompressible Euler equations, accepted by *J. Nonlinear Science* (2006).
[20] W. E & C. Shu, Small-scale structures in Boussinesq convection, *Phys. Fluids* **6**, 49 (1994).
[21] D. Chae & N.Kim, On the breakdown of axisymmetric smooth solutions for the 3-D Euler equations, *Commun. Math. Phys.* **178**, 391 (1996).
[22] D. Chae and H.S. Nam, Local existence and blow-up criterion for the Boussinesq equations, *Proc. Roy. Soc. Edinb. A* **127**, 935 (1997).
[23] W.T.Ashurst, & D.I.Meiron, Numerical study of vortex reconnection, *Phys. Rev. Lett.* **58**, 1632 (1987).
[24] R.M. Kerr & F. Hussain, Simulation of vortex reconnection, *Phys. D* **37**, 474 (1989).
[25] H.K. Moffatt, The interaction of skewed vortex pairs: a model for blow-up of the Navier-stokes equations, *J. Fluid Mech.* **409**, 51 (2000).
[26] R. Grauer & T.C. Sideris, Numerical computation of 3D incompressible ideal fluids with swirl, *Phys. Rev. Lett.* **67**, 3511 (1991).
[27] A. Pumir & E.D. Siggia, Collapsing solutions to the 3-D Euler equations, *Phys. Fluids A* **2**, 220 (1990).
[28] A. Pumir & E.D. Siggia, Finite-time singularities in the axisymmetric three-dimension Euler equations, *Phys. Rev. Lett.* **68**, 1511 (1992).
[29] A. Pumir & E.D. Siggia, Development of singular solutions to the axisymmetric Euler equations, *Phys. Fluids A* **4**, 1472 (1992).
[30] R. Grauer & T.C. Sideris, Finite time singularities in ideal fluids with swirl, *Phys. D* **88**, 116 (1995).
[31] L.A. Carmack, Vorticity amplification in incompressible ideal swirling flow without a boundary, *Phys. Fluids* **9**, 1379 (1997).
[32] H.D. Ceniceros & T.Y. Hou, An efficient dynamically adaptive mesh for potentially singular solutions, *J. Comput. Phys.* **172**, 609 (2001).
[33] D.L. Meiron, G.R. Baker & S.A. Orszag, Analytic structure of vortex sheet dynamics, part I. Kelvin-Helmholtz instability, *J. Fluid Mech.* **114**, 283 (1982).
[34] R.B. Pelz & Y. Gulak, Evidence for a real time singularity in hydrodynamics from time series analysis, *Phys. Rev. Lett.* **79**, 4998 (1997).
[35] R.B.Pelz, Extended series analysis of full octahedral flow: numerical evidence for hydrodynamics blowup, *Fluid Dyn. Res.* **33**, 207 (2003).
[36] Y. Gulak & R.B. Pelz, High-symmetry Kida flow: time series analysis and resummation, *Fluid Dyn. Res.* **36**, 211 (2005).
[37] D.W. Moore, The spontaneous appearance of a singularity in the shape of an evolving vortex sheet, *Proc. R. Soc. Lond. A* **365**, 105 (1979).

[38] A. Bhattacharjee & X.G. Wang, Finite-time vortex singularity in a model of three-dimensional Euler flows, *Phys. Rev. Lett.* **69**, 2196 (1992).

[39] A. Bhattacharjee, C.S. Ng & X.G. Wang, Finite-time vortex singularity and Kolmogorov spectrum in a symmetric three-dimensional spiral model, *Phys. Rev. E* **52**, 5110 (1995).

[40] C.S. Ng & A. Bhattacharjee, Sufficient condition for a finite-time singularity in a high-symmetric Euler flow: analysis and statistics, *Phys. Rev. E* **54**, 1530 (1996).

[41] J.M. Greene & O.N. Boratav, Evidence for the development of singularities in Euler flow, *Phys. D* **107**, 57 (1997).

[42] J.M. Greene & R.B. Pelz, Stability of postulated, self-similar, hydrodynamic blowup solutions, *Phys. Rev. E* **62**, 7982 (2000).

[43] V.P.Ruban, D.I. Podolsky & J.J.Rasmussen, Finite time singularities in a class of hydrodynamic models, *Phys. Rev. E* **63**, 056306 (2001).

[44] K. Ohkitani & J.D. Gibbon, Numerical study of singularity formation in a class of Euler and Navier-Stokes flows, *Phys. Fluids* **12**, 3181 (2000).

[45] J.D. Gibbon & K. Ohkitani, Singularity formation in a class of stretched solutions of the equations for ideal magneto-hydrodynamics, *Nonlinearity* **(**14), 1239 (2001).

[46] J.D. Gibbon, D. R. Moore & J.T. Stuart, Exact, infinite energy, blow-up solutions of the three-dimensional Euler equation, *Nonlinearity* **(**16), 1823 (2003).

[47] P. Santangelo, R. Benzi & B. Legras, The generation of vortices in high-resolution, two-dimensional decaying turbulence and the influence of initial conditions on the breaking of self-similarity, *Phys. Fluids* A **1**, 1027 (1989).

[48] P. Constantin, A.J. Majda & E.G. Tabak, Singular front formation in a model for quasi-geostrophic flow, *Phys. Fluids* **6**, 9 (1994).

[49] A.J. Majda & E.G. Tabak, A two-dimensional model for quasigeostrophic flow: comparison with the two-dimensional Euler flow, *Phys. D* **98**, 515 (1996).

[50] J.C. McWilliams, I. Yavneh, M.J.P. Cullen & P.R. Gent, The breakdown of large-scale flows in rotating, stratified fluids, *Phys. Fluids* **10**, 3178 (1998).

[51] U. Frisch, T. Matsumoto & J. Bec, Singularities of Euler flow? Not out of the blue! *J. Stat. Phys.* **113**, 761 (2003).

[52] T. Matsumoto, J. Bec & U. Frisch, The analytic structure of 2D Euler flow at short times, *Fluid Dyn. Res.* **36**, 221 (2005).

[53] S.A. Orszag, Numerical simulation of incompressible flows within simple boundaries. I. Galerkin (spectral) representations, *Stud. Appl. Math.* **50**, 293 (1971).

[54] C. Canuto, M.Y. Hussaini, A. Quarteroni, and T.A. Zang, *Spectral methods in fluid dynamics*, Springer, New York, Berlin, 1987.

[55] Z. Yin, H.J.H. Clercx, & D. Montgomery, An easily implemented task-based parallel scheme for the Fourier pseudo-spectral solver applied to 2D Navier-Stokes turbulence, *Comput. Fluids* **33**, 509 (2004).

[56] Z. Yin, L. Yuan & T. Tang, A new parallel strategy for two-dimensional incompressible flow simulations using pseudo-spectral methods, *J. Comput. Phys.* **210**325 (2005).

[57] P. Dmitruk & D.C. Montgomery, Numerical study of the decay of enstrophy in a two-

dimensional Navier-Stokes fluid in the limit of very small viscosities, *Phys. Fluids* **17**, 035114 (2005).

[58] G.S. Patterson & S.A. Orszag, Spectral calculations of isotropic turbulence: Efficient removal of aliasing interaction, *Phys. Fluids* **14**, 2538 (1971).

[59] H. Vandeven, Family of spectral filters for discontinuous problem, *J. Sci. Comput.* **6**, 159 (1991).

[60] C.W. Shu, W.S. Don, D. Gottlieb, O. Schilling & L. Jameson, Numerical convergence study of nearly incompressible inviscid Taylor-Green vortex flow, *J. Sci. Comput.* **24**, 1 (2005).

[61] R. Krasny, A study of singularity formation in a vortex sheet by the point-vortex approximation, *J. Fluid Mech.* **167**, 65 (1986).

[62] R. Krasny, Computation of vortex sheet roll-up in the Trefftz plane, *J. Fluid Mech.* **184**, 123 (1987).

[63] M. Tasche & H. Zeuner, Worst and average case roundoff error analysis for FFT, *BIT* **41**, 563 (2001).

[64] J.C. Schatzman, Accuracy of the discrete Fourier transform and the fast Fourier transform, *SIAM J. Sci. Comput.* **17**, 1150 (1996).

[65] C.D. Cantrell, *Modern mathematical methods for physicists and engineers* (Cambridge, 2000).

[66] U. Frisch, *Turbulence* (Cambridge, 1995).

[67] The location of $|\nabla\theta|_{max}$ will cross the boundary at $t \approx 3.2$, so we measure the distance on the $[0, 2\pi] \times [1.5, 1.5 + 2\pi]$ domain instead of on $[0, 2\pi] \times [0, 2\pi]$.